International Journal of Heat and Mass Transfer 204 (2023) 123834

Contents lists available at ScienceDirect

International Journal of Heat and Mass Transfer

journal homepage: www.elsevier.com/locate/hmt

Experimental analysis of forced convective heat transfer of nitrate salt in a spirally grooved tube at high Reynolds numbers and temperatures

Cathy Frantz[a,*], Reiner Buck[a], Marc Röger[b], Bernhard Hoffschmidt[c,d]

[a] German Aerospace Center (DLR) Stuttgart, Germany
[b] German Aerospace Center (DLR) Almeria, Spain
[c] German Aerospace Center (DLR), Institute of Solar Research, Germany
[d] RWTH Aachen University, Chair of Solar Components, Germany

ARTICLE INFO

Article history:
Received 21 October 2022
Revised 11 December 2022
Accepted 30 December 2022

Keywords:
Forced convective heat transfer
Nusselt number
Solar Salt
Nitrate salt
Solar receiver
CSP
Nuclear
Spirally grooved tube
Enhanced tube
Corrugated tube
Induction heater
Measurement setup
Pressure difference

ABSTRACT

The forced convective heat transfer and pressure difference of molten nitrate salt in a spirally grooved tube with a relative groove height $e/2r_i$=0.017, a relative groove pitch $p/2r_i$ =0.913 and groove angle α=73.8° is experimentally investigated using a water-cooled induction heater setup. The data is provided for Reynolds numbers ranging between 11000 up to 285000 and Prandtl numbers from 3.7 to 10. The experiments are carried out for bulk salt temperatures ranging between 300 and 550 °C and for heating flux densities between 330 and 930 kW/m². Inner wall temperatures up to 633 °C are achieved with the setup, thus providing data on the behavior of the forced convective heat transfer as a function of inner wall temperature. The data is compared to the measurement results obtained with the same setup and a circular smooth tube as well as correlations and data from the literature in order to deduce relative Nusselt numbers and friction factors.

© 2023 Elsevier Ltd. All rights reserved.

1. Introduction

Over the last decades molten nitrate salts have become a popular candidate both as a high temperature heat storage and heat exchanger fluid because of their relatively high heat capacity, low vapor pressure, low cost and relatively good availability [1]. The binary mixture of 60% sodium nitrate ($NaNO_3$) and 40% potassium nitrate (KNO_3) is solid at ambient temperature, nontoxic and non-flammable. It has its melting point at roughly 238 °C and is chemically stable up to roughly 600 °C with ambient air as the cover gas [2]. It is commonly applied in concentrating solar power (CSP) systems such as solar towers both as a heat transfer and storage medium. The so-called Solar Salt exposes a low thermal conductivity, which minimizes heat losses in thermal storage applications. However, the same property leads to low forced convective heat transfer coefficients in heat exchangers, which again limits the allowable heat flux through the tubes. In tubular central tower receivers high heat fluxes up to > 1 MW/m² are desirable to minimize heat exchanger size and thus heat exchanger costs [3]. As a consequence, high flow velocities are employed in nitrate salt tubular heat exchangers. This commonly leads to Reynolds numbers larger than 200′000 in smooth tubes in order to achieve the desired high forced convective heat transfers [4]. On the other hand, this practice leads to high pressure drops in the heat exchanger and consequently high pumping costs. One approach to increase the performance of heat exchangers, while minimizing pumping costs, is to enhance the convective heat transfer by the usage of passive augmentation methods [5].

Solar Salt is chemically active above temperatures of 400 °C with at first an equilibrium reaction between nitrate and nitrite ions with gaseous oxygen [6]. Above 550 °C, several further decomposition reactions of the nitrite ion are known to occur [6]. All of them propose the formation of oxide ions together with different gaseous species (e.g., NO, NO_2, O_2, N_2) [7]. One concern is that localized decomposition of the nitrate salt in the film region with formation of gaseous products would

* Corresponding author.
E-mail address: cathy.frantz@dlr.de (C. Frantz).

https://doi.org/10.1016/j.ijheatmasstransfer.2022.123834
0017-9310/© 2023 Elsevier Ltd. All rights reserved.

Nomenclature

c_p	Specific heat capacity (J/kg/K)
ρ	Density (kg/m³)
λ	Thermal conductivity (W/(mK))
R	Universal gas constant (J/(Kmol))
Re	Reynolds number (-)
Pr	Prandtl number at bulk temperature (-)
$Pr_{t,i}$	Prandtl number at inner tube wall temperature (r=r_i) (-)
Nu_x, Nu_m	(x): Nusselt number at the location x (-); (m): Mean Nusselt number over heating section (-)
T	Temperature (°C)
$\dot{m}_{cw}$; $\dot{m}_S$	Mass flow of cooling water (cw); mass flow main fluid solar salt (s) (kg/s)
U_{RMS}; I_{RMS}; φ	Active voltage (V); active current (A); phase shift (rad)
P	Power (W)
ϕ	Volumetric heating density of the tube (W/m³)
$\dot{q}$	Flux density (W/m²)
r_i; r_o	i: inner radius tube test section; o: outer radius tube test section (m)
t	Thickness (m)
l_{heat}	length of heated tube (m)
V	Volume (m³)
e, p, α	Geometry enhanced tube: e: groove height (m), p: groove pitch (m), α: pitch angle (°)
f	Friction factor

Subscripts

s	Solar Salt (60 wt-% $NaNO_3$, 40 wt-% KNO_3)
t	Test tube
cw	Cooling water
ins	Insulation between test tube and induction heater
i; o	i: property at inner radius tube test section; o: property at outer radius tube test section
x	property at axial position along heating section
in; out	in: property at flow inlet; out: property at flow outlet
a	Enhanced tube
0	Smooth tube
per	Peripheral components

form a local gas layer with low thermal conductivity and that his layer would negatively impact the convective heat transfer of Solar Salt in heat exchanger tubes. A decrease of convective heat transfer would then again lead to an increase in film temperatures and would probably entail further acceleration of the decomposition process. The geometry of enhanced tubes do not only cause a local increase of fluid velocity but can also induce wakes and low-speed recirculation zones involving a local decrease in fluid velocity [8]. This could cause local overheating, entail local salt degradation and consequently impact the overall convective heat transfer.

However, so far, no experimental research is available about the forced convective heat transfer and friction factor behavior of molten salt in enhanced tubes for the required high Reynolds numbers and temperatures in tubular central tower receivers. Furthermore, no research has been published on the impact of film temperature above the chemical stability limit of Solar Salt on the forced convective heat transfer in enhanced tubes. This paper presents experimental data of the mean Nusselt number and friction factor of Solar Salt in a spirally grooved tube at Re>10′000 up to film temperatures of 633 °C and compares it to data from the literature.

2. State of the art of forced convective heat transfer of enhanced tubes

For today's engineering practice, sixteen different enhancement techniques have been identified [9]. These techniques can be broadly classified in passive and active methods. Passive methods to enhance the forced convective heat transfer in a tube have been employed in various industrial fields such as desalination or power plant condensers and have been widely investigated in the literature [10]. Two main passive approaches can be distinguished: 1) Methods implying the deformation of the tube (rough surfaces or extended surfaces trough transverse or helical ribs or fins); 2) insertion of structures into the tube that disturb the fluid flow (displaced enhancement devices or swirl flow devices, such as twisted tapes or wire coils) [11]. The main idea behind these approaches is the disturbance of the existing boundary layer, increase of heat transfer area, increased turbulence of the flow or a combination of all three, which leads to an increased heat-transfer performance. The most successful technique, mainly because of its effectiveness and simplicity in application, has been augmentation through surface roughness [11]. Here the surface roughness of the tube is increased by forming repeated grooves in the tube. These grooves create a disturbance of the laminar sublayer in the near-wall turbulent flow and as a consequence increase the forced convective heat transfer. The most common groove pattern for large scale production is a helical groove pattern because it allows a continuous fabrication process through rolling or indenting [12]. Fig. 1 shows the definition of the main geometric parameters groove height e, groove pitch p and helix angle of groove α. Generally, both the Nusselt number and the friction factor increase for decreasing groove pitch, increasing groove height and higher helix angles. Of these three factors, the groove height e has the strongest impact [12]. The groove height affects the separation of the boundary layer by vortex and jet generation. The groove pitch restrains the boundary layer development and thus leads to thinner boundary layers. However, it was observed that for small pitches sluggish and stagnant vortex can occur, which lowers the heat transfer [13]. Other factors, such as groove shape or groove width are found to play a minor role in the heat transfer increase [14].

Numerous investigations have been published in the past about the heat transfer and friction factor of fluids in enhanced tubes [15]. As the present experimental results are generated for single-phase forced convective flow in a rough surface or corrugated tube [10], the presented literature is limited to the work performed on this type of enhancement. Furthermore, the published work on wire coil inserts is included because several authors consider that wire coil inserts disturb turbulent flow in an analogous fashion to grooved tubes [12,16]. In a first step an overview over past and current research involving all fluids is given. In a second step the available research on the enhanced heat transfer using molten salts is presented and analyzed in more detail.

In 1971, Webb et al. published correlations based on experimental data for transverse grooves [17], while Gee and Webb presented correlations for helical ribs in 1980 [18]. In 1982, Li et al. developed correlations for helical ribs which also include the impact of groove pitch length and groove angle [19]. In 1996, Ravigururajan and Bergles developed general correlations for the friction factor and heat-transfer coefficient for single-phase turbulent flow of Newtonian fluids in internally augmented tubes. They verified their correlations for a wide range of tube parameters with $e/2r_i$=0.01 to 0.2; $p/2r_i$=0.1 to 7.0 and $\alpha/90$=0.3 to 1.0 using experimental data from seventeen authors. (>1650 datapoints for pressure drop, 1800 data points for heat transfer) The collected experimental data was collected for Re numbers ranging between 5000 up to 250,000 and Pr ranging between 0.66 up to 37.6. Most of the studies of the database used water or air as the working fluid. Their deduced cor-

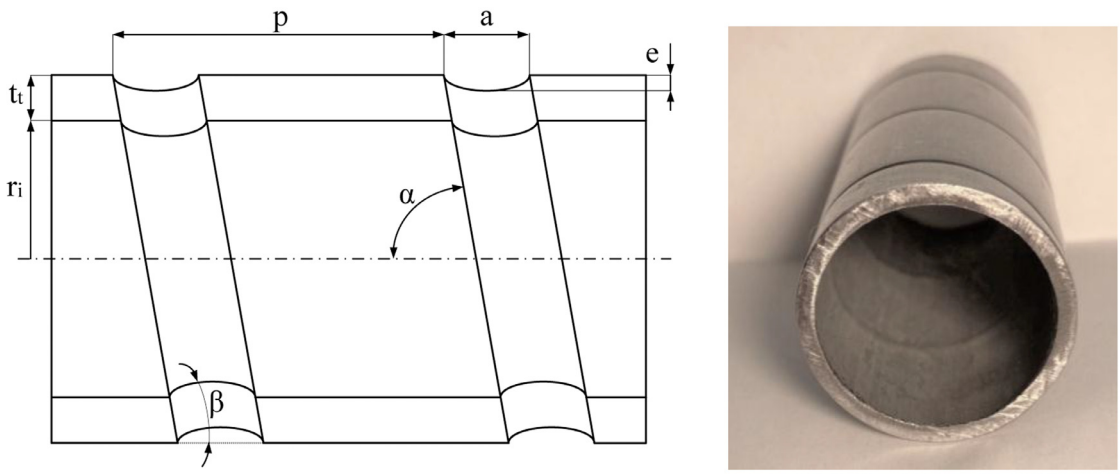

Fig. 1. Left: Geometry definition of spirally grooved tube; Right: Specimen of the test tube used in this work.

relation predicts 96% of the friction factor database and 99% of the Nusselt number database to within ±50%. 77% of the friction factor and 69% of the Nusselt number database are predicted within ±20% [12]. The following two equations show the resulting correlations for the expected ratios of friction factor f_a/f_0 and Nusselt number Nu_a/Nu_0 [10]:

$$\frac{f_a}{f_0} = \left\{ \left[29.1 \cdot Re^{0.67-0.06\cdot p/d-0.49\cdot\alpha/90} \cdot \left(\frac{e}{2r_i}\right)^{1.37-0.157\cdot p/d} \cdot \left(\frac{p}{2r_i}\right)^{-1.66e^{-6}\cdot Re-0.33\cdot\alpha/90} \cdot \left(\frac{\alpha}{90}\right)^{4.59+4.11e^{-6}\cdot Re-0.15\cdot\frac{p}{d}} \cdot (1+(2.94\cdot sin\beta)/n) \right]^{15/16} \right\}^{16/15} \quad (1)$$

$$\frac{Nu_a}{Nu_0} = \left\{ 1 + \left[2.64 \cdot Re^{0.036} \left(\frac{e}{2r_i}\right)^{0.212} \cdot \left(\frac{p}{2r_i}\right)^{-0.21} \cdot \left(\frac{\alpha}{90}\right)^{0.29} \cdot \mathrm{Pr}^{-0.024} \right]^7 \right\}^{1/7} \quad (2)$$

Where β is the contact angle in degrees of the roughness profile relative to the flow direction and is taken as 90° (semi-circular profiles [12]) and n denotes the number of spiral rib starts.

In 2005, Garcia et al. presented experimentally deduced correlations for the convective heat transfer and friction factor for flow enhancement using wire coil inserts in laminar-transition-turbulent regimes for Prandtl numbers ranging between 2.8 and 150 and Reynolds numbers ranging from 80 to 90,000. They were able to show, that wire coil inserts maximize their impact in transitional flow regimes [20]. In 2015, Ji et al. published a review on the available literature on single-phase heat transfer enhancement techniques of liquid laminar and turbulent pipe flow [21]. They summarized the work of a total of 13 authors, which have published experimental data on the thermo-hydraulic performance of corrugated tubes for Reynolds numbers ranging between 100 and 100,000 between the years of 1977 and 2015. The review also contained the work of two authors who evaluated wire coil inserts. The experimental data was obtained with setups using water or oil. The evaluation of the thermo-hydraulic performance was performed following the approach proposed by Fan et al. [22]. Ji et al. summarized that an enhanced heat transfer of corrugated tubes can regularly be obtained with an identical pressure drop. The wire coil inserts in this study showed enhanced heat transfer per identical pumping power or identical pressure drop. In 2017, Ji et al. performed a detailed review on several types of enhancement techniques for laminar and turbulent air flow [23]. The reviewed data for wire coil inserts included six studies for Reynolds numbers ranging between 100 and 45,000. Ji summarized that heat transfer augmentation ratios through inserts for gasses are in the range of 2–4 and friction factor increment ratios are higher than the heat transfer [23]. Furthermore, Ji et al. summarized the work of 11 authors who studied the thermo-hydraulic performance of different corrugated tubes over a Reynolds number ranging between 2000 and 100,000. Ji et al. found that an enhanced heat transfer of corrugated tubes can regularly be obtained with the identical pressure drop and that the heat transfer ratios for gasses a very similar to liquid, while pressure drop penalties for gasses are considerably higher [23]. The next paragraphs give an overview over the available experimental and simulation data on molten salt in corrugated tubes.

In 2013, Jiangfeng et al. published their results of the convective heat transfer of the ternary nitrate salt Hitec ($NaNO_3$–$NaNO_2$–KNO_3, 7–40–53 wt.%) for salt temperatures ranging between 250 and 500 °C and for Reynolds numbers between 10,000 and 30,000 [24]. They compared their results of a smooth tube to three different transversely grooved tubes ($\alpha/90$=1) with groove heights of $e/2r_i$=0.038; 0.046 and 0.092 and a relative groove pitch $p/2r_i$=0.738. They fitted a correlation to their measurement data, which indicates that the Nusselt number can be increased 1.8 times for $e/2r_i$=0.092. No measurements of the pressure difference are published. The same year, Jiangfeng et al. published results of the convective heat transfer of the same molten salt for Reynolds numbers between 5000 and 15,000 for spirally grooved tubes. Their measurement campaign was performed on four different tubes with a pitch angle of 78°, relative groove pitch of $p/2r_i$=0.738 and the following relative groove heights: $e/2r_i$=0.024, 0.031, 0.038 and 0.048. They found that the measured Nusselt number increases up to 1.4–1.7 times compared to a smooth tube for the highest relative groove height [25]. An updated correlation for their measurement data was published by Jiangfeng in 2015 [26]. No pressure difference is published. Also, the same year, Chen et al. published their results on enhanced tubes with Hitec salt for the Reynolds number range 10,000–30,000 [27]. They analyzed three transversally grooved tubes ($\alpha/90$=1) with a relative groove pitch ranging between $p/2r_i$=0.31–1 and relative groove heights ranging between 0.55 and 0.75. They found that no relevant increase of the Nusselt number is found for a relative groove pitch $p/2r_i$=1. For the two tubes with lower relative tube pitch they fitted two correlations over their measurement data; these fits lead

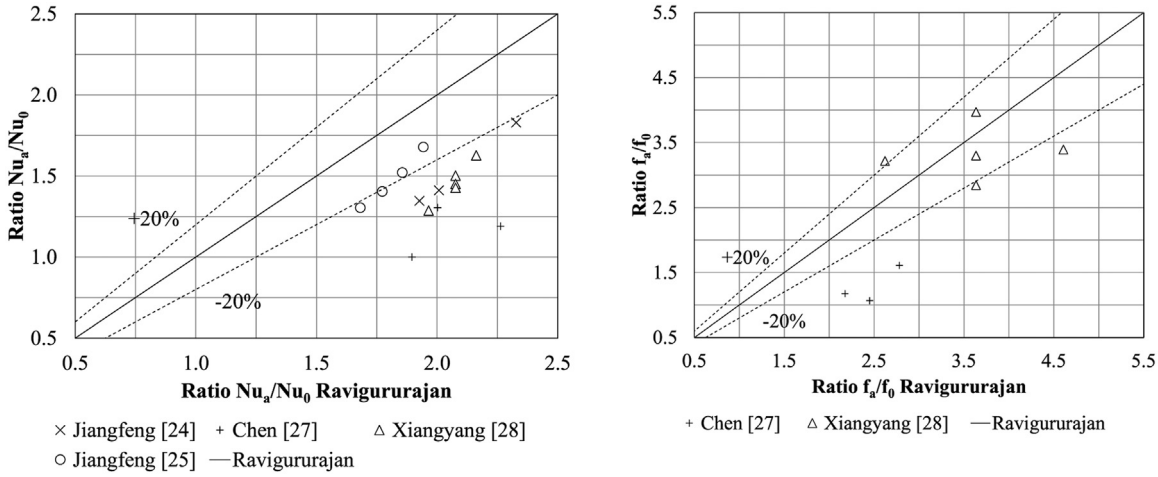

Fig. 2. Nusselt number ratio (left) and friction factor ratio (right) of different authors [24,25,27,28] compared to the respective ratios predicted by the general correlation [10].

Table 1
Correlations and geometric specifications from the literature.

Source	Correlation author	$\alpha/90$	$e/2r_i$	$p/2r_i$
Jiangfeng, [24]	$\frac{Nu_a}{Nu_0} = \frac{0.0301Re^{0.796} \cdot Pr^{1/3}(1+\frac{2e}{d})^{3.18}}{0.027Re^{0.8} \cdot Pr^{1/3}}$	1	0.038	0.738
		1	0.046	0.738
		1	0.092	0.738
Jiangfeng, [26]	$\frac{Nu_a}{Nu_0} = \frac{0.02762Re^{0.798} \cdot Pr^{1/3}(1+\frac{2e}{d})^{5.68}}{0.027Re^{0.8} \cdot Pr^{1/3}}$	0.867	0.048	0.738
		0.867	0.038	0.738
		0.867	0.031	0.738
		0.867	0.024	0.738
Chen, [27]	$\frac{Nu_a}{Nu_0} = 1;\ \frac{f_a}{f_0} = \frac{0.14Re^{-0.029 \cdot Pr^{1/3}}}{0.13Re^{-0.028} \cdot Pr^{1/3}}$	1	0.047	1.000
	$\frac{Nu_a}{Nu_0} = \frac{0.03524Re^{0.8} \cdot Pr^{1/3}}{0.027Re^{0.8} \cdot Pr^{1/3}};\ \frac{f_a}{f_0} = \frac{0.28Re^{-0.087}}{0.13Re^{-0.028}}$	1	0.034	0.563
	$\frac{Nu_a}{Nu_0} = \frac{0.03213Re^{0.8} \cdot Pr^{1/3}}{0.027Re^{0.8} \cdot Pr^{1/3}};\ \frac{f_a}{f_0} = \frac{0.54Re^{-0.12}}{0.13Re^{-0.028}}$	1	0.034	0.313
Xiangyang, [28]	Simulation results	1	0.046	0.819
		1	0.059	0.819
		1	0.072	0.819

to an increase of 1.2 to 1.3 times of the Nusselt number relative to a smooth tube. They also deduced a general correlation, but this correlation does not account for the impact of groove pitch on the Nusselt number, so it will not be further considered. They also compared the measured pressure difference of the different tubes and fitted correlations for each tube. It can be found that the friction factor is increased by a factor of 1.07 to 1.19. Xiangyang et al. developed a CFD model for transversely grooved tubes and validated the model using experimental data obtained with the nitrate salt Hitec [28]. The final simulation studied the heat transfer of different transversely grooved tubes ($\alpha/90$=1) for three relative groove heights under non-uniform radiation and deduced a correlation for the Nusselt number. Furthermore, they varied the groove width p and confirmed that the impact of groove width on the Nusselt number was lower than the impact of the groove height e. Fig. 2 shows the ratios of Nusselt number (left) and friction factor (right) deduced by the above-mentioned authors compared to the general correlations from Ravigururajan. The respective ratios are deduced using the author correlations (see Table 1) compared to the Sieder-Tate-correlation [29]. In this analysis the impact of the ratio of dynamic viscosity $(\mu/\mu_w)^{0.14}|_a/(\mu/\mu_w)^{0.14}|_s$ is neglected, as its impact is lower than a few percent. It can be observed that the general correlations overpredict the measured Nusselt number ratio by 15% up to 90%. Better agreement is found for the data of the relative friction factor of the simulation of Xiangyang et al. The friction factor ratio of the experimental data of Chen et al., however is overpredicted by a factor 1.7 up to 2.3.

Based on the available experimental data the following conclusions can be made: general correlations are available for the relevant Reynolds number and Prandtl number range. However, the available experimental data for molten salts is limited to Reynolds numbers up to 30,000. This is considerably lower than the Reynolds number used for example in concentrating solar power (CSP) applications, which are commonly operated at Reynolds numbers ranging between 10,000 and more than 200,000 [4]. Also, compared to the experimental data, the general correlations overpredict the measured Nusselt number ratio of other authors by up to 90% and the friction factor ratio by up to more than a factor of two.

3. System description

The used test setup to experimentally deduce the Nusselt number and friction factors is shown in Fig. 3. The heating section is designed using a cylindrical induction heater. 2 × 3 type N thermocouples measure the main fluid inlet and outlet temperature. The heating section is equipped with 32 type N thermocouples, which are welded to the outer tube wall using a micro laser beam weld. The cylindrical induction heater is water-cooled during operation in order to prevent overheating at high loads. The cooling water inlet and outlet temperature is obtained by 2 × 3 type K thermocouples. These thermocouples are electrically insulated by a Fluorinated-ethylene-propylene coating. All thermocouples are calibrated using an Ametek ATC650B dry block calibrator. A Heinrichs TMU-010 Coriolis sensor is used to measure the cooling water mass flow. The root mean square current of the induction heater is measured using a Chauvin-Arnoux MA-200 Rogowski coil, the root mean square (RMS) voltage by an R&S RT-ZI10 passive probe. Both signals are monitored and processed using an R&S RTH1002 oscilloscope. The whole test section is insulated using silica fiber wool. Table 2 summarizes the geometric specifications of the test section. The described test section is implemented into the TESIS:com plant in Cologne, Germany (see Figs. 4 and 5) [30]. The TESIS:com testing facility consists of a hot and a cold molten salt tank, each able to contain 20 t of Solar Salt. The salt can be heated or cooled to the desired temperature ranging between 290 and 560 °C and

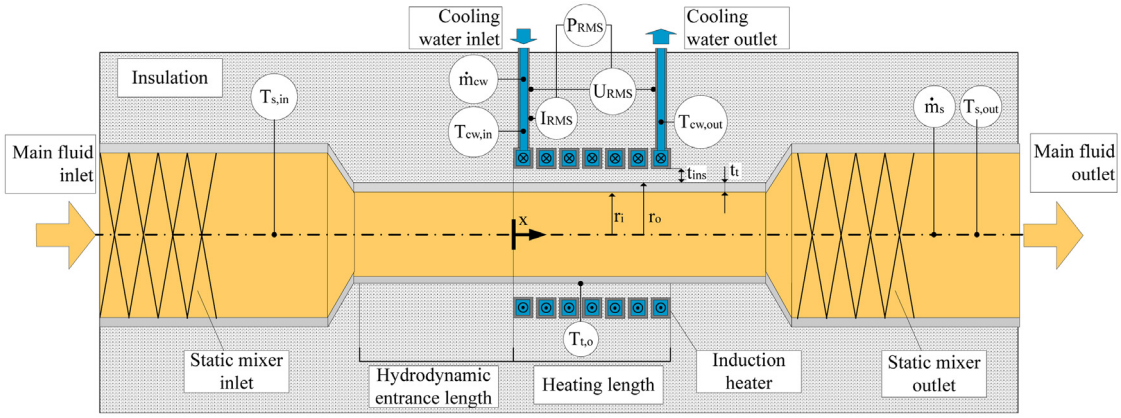

Fig. 3. Schematic representation of the main test section.

Table 2
Geometric specifications main test section.

Parameter	Value
Outer diameter tube $2 \cdot r_o$	26.9 ± 0.3 mm
Tube wall thickness t_t	2 ± 0.2 mm
Hydrodynamic entrance length	1250 mm
Heating length l_{heat}	470 mm ±18 mm
Thickness insulation between induction heater and tube test section t_{ins}	15 mm ±5 mm
Outer insulation thickness	~300 mm
Coil inner diameter $2 \cdot r_{ind}$	60 mm
No of turns per m solenoid heating coil	72 turns/m
Groove height e	0.4 mm ±0.05 mm
Pitch length p	20.9 mm ±0.1 mm
Groove width a	1.8 mm ±0.2 mm
Pitch angle α	73.8°
Equivalent diameter spirally grooved tube d_H	22.8 mm

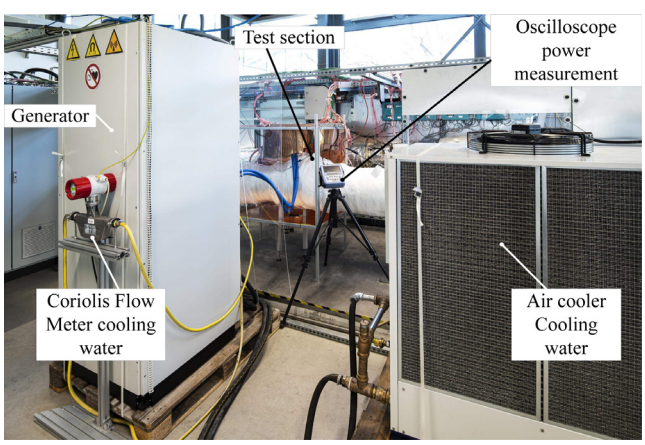

Fig. 4. Test setup.

can then be pumped with different mass flows through the test section. One $E + H$ Micropilot FMR54 radar level sensor is positioned at the top of each salt tank. These sensors are used to deduce the mean mass flow of the salt through the test section. The radar sensors are calibrated using a Coriolis sensor and water. The tank deformation and the resulting uncertainty at higher temperature has been simulated using a detailed FEM simulation of the tank and the salt. Furthermore, the instantaneous solar salt mass flow is measured using three serially placed FLEXIM WI-400 ultrasonic clamp-on mass flow sensor. The salt mass flow measurement approach is validated for the use with Solar Salt up to 400 °C using a high temperature KROHNE Optimass 6400 Coriolis sensor. A generator provides the power for the induction heater. The cooling water circuit is cooled using an air to water cooler. The whole setup is validated by a test campaign with water. A more detailed description of the measurement setup as well as the smooth tube results

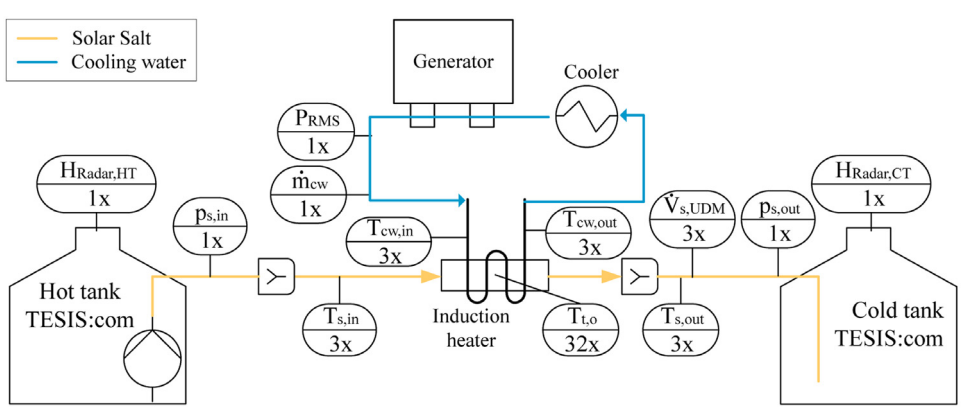

Fig. 5. Experimental system diagram Solar Salt loop.

can be found in [31]. The pressure difference over the test section is measured before and after the test section using an $E+H$ PMP75 pressure transmitter with a diaphragm seal at the salt inlet and a Gems Sensors & Controls 3500 series pressure transducer with an air blanket at the salt outlet.

4. Theoretical basis

4.1. Nusselt number

This subchapter is a shortened repetition of the theoretical basis described in [31] added for better readability of this paper. The Fourier law of heat transfer in a cylindrical system is used to deduce the general local stationary heat balance (Eq. (3)) [32]. Two boundary conditions are applied to this heat balance: Heat losses through the insulation of the tube to the induction heater (see Eq. (4)) and convective heat transfer to the molten salt at the inner side of the tube (Eq. (5)).

$$\frac{1}{r}\frac{d}{dr}\left(r\frac{dT_{t,x}}{dr}\right)+\frac{\phi}{\lambda_t}=0 \tag{3}$$

$$-\lambda_t\cdot\frac{d}{dr}T_{t,x}(r)|_{r=r_o}=\dot{q}_{ins} \tag{4}$$

$$-\lambda_t\cdot\frac{d}{dr}T_{t,x}(r)|_{r=r_i}=-\frac{Nu_{s,x}\cdot\lambda_s}{2r_i}\cdot(T_{t,x}(r=r_i)-T_{s,x}) \tag{5}$$

In order not to disturb the inner fluid flow, the tube temperature is measured at the location r=r_o. In a next step, the temperature at $T_t(r=r_o)$ is inserted and the equation system is solved for $Nu_{s,x}$:

$$Nu_{s,x}=\frac{4\lambda_t\left[\phi\left(r_o^2-r_i^2\right)-2r_o\dot{q}_{ins}\right]}{\lambda_s\cdot\left[4\lambda_t(T_{t,o,x}-T_{s,x})+2r_o ln\left(\frac{r_o}{r_i}\right)(2\dot{q}_{ins}-\phi r_o)+\phi\left(r_o^2-r_i^2\right)\right]} \tag{6}$$

All material properties of the salt are evaluated at mean bulk salt temperature. The volumetric inductive heating density of the tube is defined with $\phi=P_t/V_{tube}$. Two measurement approaches are used to deduce the power transferred by the induction heater to the tube: for the first approach the energy balance about the main fluid flow is set up according to Eq. (7). This approach will be referred to as the "calorimetric method".

$$P_{t,cal}=\dot{m}_s\cdot\bar{c}_{p,s}\left(\bar{T}_s\right)\cdot(T_{s,out}-T_{s,in})+\frac{\lambda_{ins}}{r_o\cdot\ln\left(\frac{r_{ind}}{r_o}\right)}\cdot 2\pi r_o\cdot l_{heat}\cdot\left(T_{t,o}-\bar{T}_{cw}\right) \tag{7}$$

Where r_{ind} is the inner radius of the induction heater. For the second approach the energy balance of the cooling water loop combined with the measurement of the active power is used according to Eq. (8). This approach will be referred to as the "electrical method".

$$P_{t,el}=U_{RMS}\cdot I_{RMS}\cdot\cos(\varphi)-\dot{m}_{CW}\cdot\bar{c}_{p,cw}\left(\bar{T}_{cw}\right)\cdot(T_{cw,out}-T_{cw,in})+\frac{\lambda_{ins}}{r_o\cdot\ln\left(\frac{r_{ind}}{r_o}\right)}\cdot 2\pi r_o\cdot l_{heat}\cdot\left(T_{t,o}-\bar{T}_{cw}\right) \tag{8}$$

Finally, the mean Nusselt number $Nu_{s,m}$ is defined as shown in Eq. (9).

$$Nu_{s,m}=\frac{\int_0^{l_{heat}}Nu_{s,x}dx}{l_{heat}}\approx\frac{1}{l_{heat}}\left[\sum_1^{n_x}Nu_{s,x}\cdot\Delta x\right] \tag{9}$$

The Nusselt number ratio is defined as the ratio of the mean Nusselt number of the spirally grooved tube and the mean Nusselt number of the smooth tube $Nu_{a,0}=Nu_a/Nu_0$.

4.2. Friction factor

The friction factor f of the test section is deduced by rearranging the general correlation for pressure difference of single-phase flow in a tube [33].

$$f=\frac{(\Delta p_{s,t})\cdot 4r_i}{l_t\rho_s u_s^2}=\frac{\left(\Delta p_{s,total}-\Delta p_{per}\right)\cdot 4\pi^2\cdot(r_o-t_t)^5\cdot\rho_s}{l_t\dot{m}_s^2} \tag{10}$$

Where Δp_{total} is the measured pressure difference between inlet and outlet and Δp_{per} is the pressure difference of all the components, but the respective test tube in between the pressure measurement (static mixer, reducer, other tubing…). l_t is the total length of the test tube, including the hydrodynamic entrance length. The friction factor ratio is defined as the ratio between the deduced friction factor of the grooved tube f_a and the smooth tube f_0. By definition, all geometric parameters can be reduced.

$$\frac{f_a}{f_0}=\frac{\left(\frac{(\Delta p_{s,total}-\Delta p_{per})\cdot\rho_s}{\dot{m}_s^2}\right)_a}{\left(\frac{(\Delta p_{s,total}-\Delta p_{per})\cdot\rho_s}{\dot{m}_s^2}\right)_0} \tag{11}$$

4.3. Reference correlation

Frantz et al. conducted measurements for a smooth tube using the same measurement setup [31]. They were able to show that the Nusselt numbers predicted using the Gnielinski correlation predict 97% of their measurement within ±10% deviation. For this reason, the Gnielinski correlation Eq. (12), ((14)) will be used for comparison of the enhanced tube results with a smooth tube [34]. Eq. (12) shows the Gnielinski correlation for the mean Nusselt number, Eq. (13) shows the Gnielinski correlation for the Nusselt number at the axial location x [33].

$$Nu_{m,REF}=\frac{\xi/8\cdot Re\cdot Pr}{1+12.7\cdot\sqrt{\xi/8}\left(\mathrm{Pr}^{2/3}-1\right)}\left[1+\left(\frac{2r_i}{l_{heat}}\right)^{2/3}\right]\left[\frac{Pr}{Pr_{t,i}}\right]^{0.11} \tag{12}$$

$$Nu_{x,REF}=\frac{\xi/8\cdot Re\cdot Pr}{1+12.7\cdot\sqrt{\xi/8}\left(\mathrm{Pr}^{2/3}-1\right)}\left[1+\frac{1}{3}\left(\frac{2r_i}{x}\right)^{2/3}\right]\left[\frac{Pr}{Pr_{t,i}}\right]^{0.11} \tag{13}$$

$$\xi=(1.8\cdot\log_{10}Re-1.5)^{-2} \tag{14}$$

The thermal entrance length has a relevant impact on the measured mean Nusselt number. However, in the measurement setup the first few centimeters of the entrance length will not be evaluated. In order to enable a correct comparison, the mean Nusselt number deduced from the experiments is compared to the expected mean Nusselt number over the test section:

$$\begin{aligned}Nu_{m,REF}&=\int_0^{l_{heat}}\frac{1}{l_{heat}}Nu_{x,REF}dx\\&=\overbrace{\int_0^{x_0}\frac{1}{x_0}Nu_{x,REF}dx}^{Nu_{m,REF,0\ldots x_0}}+\overbrace{\int_{x_0}^{l_{heat}}\frac{1}{l_{heat}-x_0}Nu_{x,REF}dx}^{Nu_{m,REF,x_0\ldots l_{heat}}}\end{aligned}$$

Solving the integral leads to the following reference correlation for the mean expected Nusselt number in the test section.

$$Nu_{m,REF,x_0\ldots l_{heat}}=\frac{1}{l_{heat}-x_0}\left[\frac{\xi/8\cdot Re\cdot Pr}{1+12.7\sqrt{\xi/8}\left(\mathrm{Pr}^{2/3}-1\right)}\left[\frac{Pr}{Pr_{t,i}}\right]^{0.11}\left[(2r_i)^{2/3}\left(\sqrt[3]{l_{heat}}-\sqrt[3]{x_0}\right)-x_0+l_{heat}\right]\right] \tag{15}$$

Table 3
Overview of correlations used for the thermophysical properties of Solar Salt and the test tube.

Description	Correlation (relative uncertainty, $k = 1$)
Specific heat capacity Solar Salt $\bar{c}_{p,S}$ in J/(kg K):	$\bar{c}_{p,S} = 1529$ (±3.3%) [31]
Density Solar Salt ρ_s in kg/m³:	$\rho_s(T/°C) = 2118 - 0.7185 \cdot (T/°C$ (±0.4%) [37]
Thermal conductivity Solar Salt λ_s in W/(m K):	$\lambda_s(T/°C) = -2.2849 \cdot 10^{-4} \cdot (T/°C + 0.54692$ (±4.2%) [38]
Dynamic viscosity Solar Salt η_s in mPa·s	$\eta_s(T/K) = 0.08703 \cdot \exp, (\frac{1,699,0.8,686,}{R\cdot,(T/,K)})$ [39]
Thermal conductivity tube (1.4878) λ_t in W/(mK)	$\lambda_t(T/°C) = 1.27551 \times 10^{-2} \cdot T$ (°C)14.7449. (±4%) [31]

5. Thermophysical properties

The nitrate salt most commonly used in high temperature CSP applications is the near-eutectic binary mixture of sodium nitrate and potassium nitrate (60 wt-% $NaNO_3$; 40 wt-% KNO_3). This salt is used during the experiments at the TESIS:com plant over a bulk salt temperature ranging between 290 °C and 565 °C. The thermophysical properties of Solar Salt in the literature are subject to relatively large scattering. It is theorized that this might be associated to the chemical activity of Solar Salt above temperatures of roughly 450 °C or its low surface tension, which leads to so-called "salt creeping" and might cause salt mass loss during experiments [35]. For the uncertainty calculations a composition tolerance of ±1 wt-% is assumed for Solar Salt. The thermophysical properties of liquid water of the cooling circuit are computed with the reference correlations published by Harvey et al. [36]. A detailed description of the selection process of the correlations listed in Table 3 can be found in [31].

6. Measurement uncertainty

The combined standard measurement uncertainty is computed using the method of propagation of uncertainty using the definitions of JCGM 100:2008. For this purpose, the partial derivative of each measured quantity is computed and the overall uncertainty is calculated based on the following general definition: $\sigma_{y(x_1,x_2\ldots x_n)} \equiv \sqrt{(\frac{\partial y}{\partial x_1})^2 \cdot \sigma_{x_1}^2 + \ldots + (\frac{\partial y}{\partial x_n})^2 \cdot \sigma_{x_n}^2}$. More information on the uncertainty can be found in [31]. A coverage factor of $k = 1$ is assumed for all values cited in this work. The measured mean Nusselt number uncertainty ranges between 8% and 41% for the calorimetric method and between 6% and 12% for the electrical method. Therefore, mainly the results yielded with the electrical method will be presented. The values from the calorimetric method will be used for plausibility checks. Table 4 gives an overview over the parameter range as well as their uncertainty. The uncertainty for the electrical method is dominated by the power measurement $P_{t,el}^{el}$, which makes up for 45% to 67% of $\sigma_{Nu_m}^{el}$. The power measurement uncertainty is strongly dominated by the uncertainty of the phase angle which accounts for roughly 77% to 89% of $\sigma_{P_{t,el}^{el}}$, followed by the RMS current uncertainty, which accounts for about 10% to 14% and the RMS voltage uncertainty, which covers about 1%. All other contributors to $\sigma_{P_{t,el}^{el}}$, such as the cooling water mass flow, heat capacity and temperature gradient ($\Delta T_{CW,max} = 15\ K$) as well as $\dot{Q}_{ins}$ amount to a contribution of less than 1%. The remaining contributors to the combined Nusselt number uncertainty $\sigma_{Nu_m}^{el}$ are the thermal conductivity of the tube σ_{λ_t} (<1% to 12%) the tube thickness t_t (<1% to 8%) the thermal conductivity of the salt λ_s (3<1% to 13%), the tube outer wall temperature $T_{t,o}$ (1% to 22%), the heating length l_{heat} (12%). and the thermal losses through the insulation $\dot{Q}_{ins}$ (2–3%). All other parameters (ΔT_s, $T_{s,in}$) make up for less than 1% of the Nusselt number uncertainty $\sigma_{Nu_m}^{el}$. The absolute values of the friction factors can be deduced with an overall uncertainty ranging between 14% and 24%.

Table 4
Range of test conditions and overall measurement uncertainty.

Item	Range	Uncertainty
Main flow salt mass flow: $\dot{m}_s$	0.56–5.59 kg/s	±2% – ±15%
Cooling water mass flow: $\dot{m}_{cw}$	0.173–0.174 kg/s	±0.06%
Solar Salt inlet temperature: $T_{s,in}$	298–554 °C	±0.2 K
Solar Salt temperature gradient ΔT_s	1.3–29.7 K	±0.2 K
Outer wall temperature $T_{w,o}$	333–667 °C	±1–9 K
Cooling water temperature gradient: ΔT_{cw}	5–15 K	±0.1 K
RMS voltage U_{RMS}	266–461 V	±0.2%
RMS current I_{RMS}	496–841 A	±1%
Pressure salt inlet $p_{s,i}$	1.11 - 3.44 bar_a	±0.01 bar_a

7. Result and discussion

7.1. Nusselt number

The forced convective heat transfer of Solar Salt in a spirally grooved tube with a relative groove height $e/2r_i$=0.017, a relative groove pitch $p/2r_i$=0.913 and groove angle α=73.8° is deduced for three main bulk salt inlet temperatures: 300 °C, 400 °C and 550 °C. This leads to bulk Prandtl numbers ranging from 10 to 3.7. At each bulk salt temperature up to 5 different mass flows are assessed. This approach leads to Reynolds numbers ranging between 11,000 and 285,000. Three different flux densities are applied for each combination of mass flow and temperature: 330 kW/m², 630 kW/m² and 930 kW/m². Fig. 6 shows the resulting mean measured Nusselt number of the spirally grooved tube for the three investigated salt bulk temperatures. As generally observed for Nusselt numbers, the Nusselt number increases for higher Reynolds numbers and decreases for lower Prandtl numbers. A correlation of the form proposed by Sieder-Tate ($Nu_m = C_0 \cdot Re^{C_1} \cdot Pr^{C_3} (\mu/\mu_w)^{0.14}$) is fitted to the obtained measurement data using a least square algorithm. The resulting correlation is shown by Eq. (16). For orien-

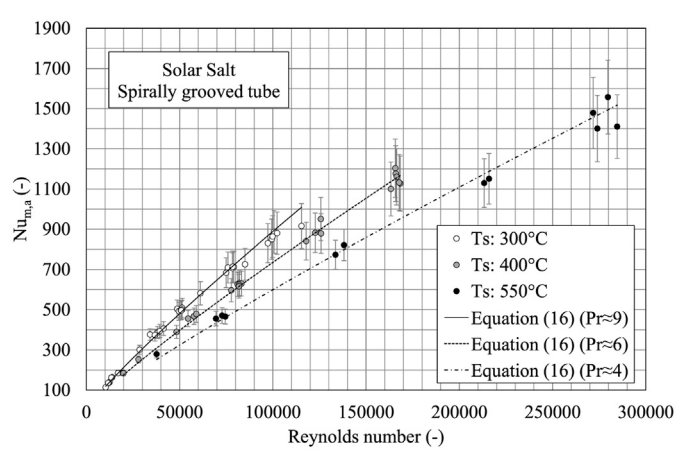

Fig. 6. Nusselt number of Solar Salt in a grooved tube as a function of Reynolds number and salt temperature (*Re*: 11,000…285,000; Pr: 3.7…10) and values calculated with Eq. (16) assuming a constant Prandtl and inner wall temperature.

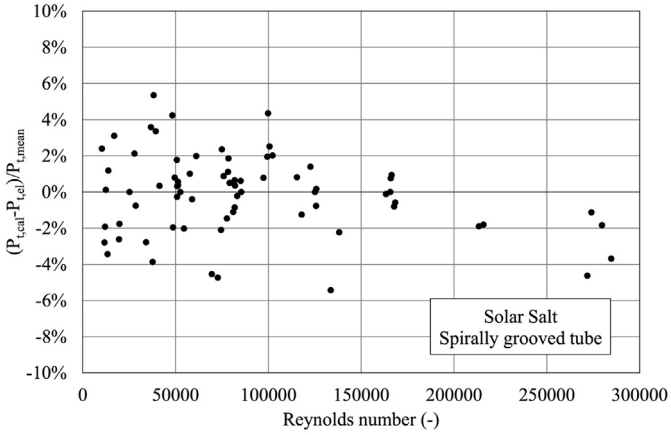

Fig. 7. Deviation of power transferred to tube using the calorimetric and the electrical method as a function of *Re* (*Re*: 11,000… 285,000; Pr: 3.7…10).

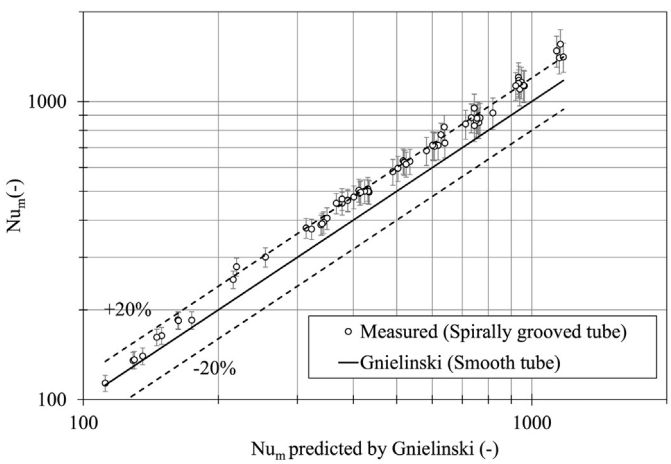

Fig. 8. Measured mean Nusselt number of Solar Salt as a function of mean Nusselt number predicted by Gnielinski correlation (*Re*: 11,000…285,000; Pr: 3.7…10).

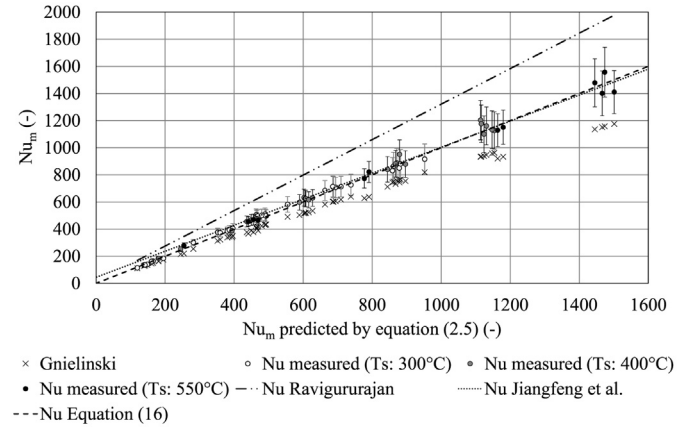

Fig. 9. Measured mean Nusselt number and mean Nusselt number predicted by several correlations as a function of the Nusselt number predicted by Eq. (16). (*Re*: 11,000…285,000; Pr: 3.7…10).

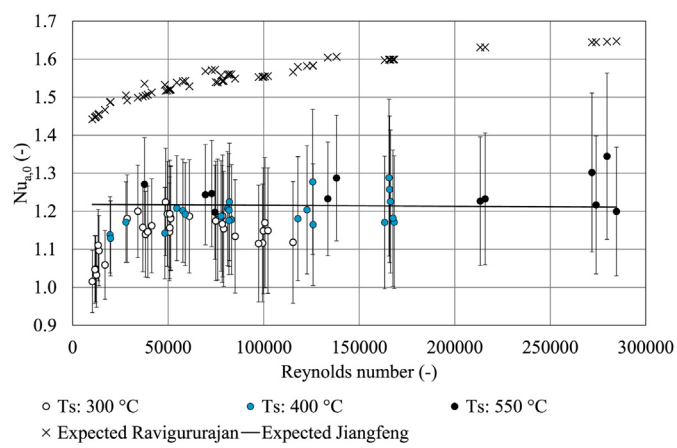

Fig. 10. Measured and expected Nusselt number ratio $Nu_{a,0}$ of two different authors as a function of Reynolds number (*Re*: 11,000…285,000; Pr: 3.7…10).

tation the fitted mean Nusselt number is shown in Fig. 6 for three representative salt bulk and inner wall temperatures.

$$Nu_{m,a} = 0.0129 \cdot Re^{0.88} \cdot Pr^{0.38} (\mu/\mu_w)^{0.14} \tag{16}$$

Fig. 7 shows the comparison of the two heat balances as a function of Reynolds number. It can be observed that 96% of the experimental cases show a deviation of less than ±5% of the "calorimetric method" – Eq. (7) - compared to the "electrical method" - Eq. (8).

Fig. 8 shows the measured mean Nusselt number of the spirally grooved tube and the mean Nusselt number predicted by the Gnielinski correlation for the smooth tube as a function of the values predicted by the Gnielinski correlation. The measured Nusselt numbers of the spirally grooved tube at Reynolds number smaller than 25,000 are only slightly higher or equal to the values predicted by Gnielinski for the smooth tube. For Reynolds numbers ranging between 27,000 up to 285,000 the measured Nusselt numbers of the enhanced tube are about 20% higher than those expected by the Gnielinski correlation for a smooth tube.

Fig. 9 shows the resulting Nusselt number ratio $Nu_{a,0}$ for all three bulk salt temperatures as a function of Reynolds number. Both graphs show the good agreement between the fitted correlation and the measurement: the fitted correlation (16) fits 79% of the measured values within ±5% and 99% of the measured values within ±8%. The same figures show the values predicted by the general correlation proposed by Ravigururajan et al. [10]. As also found by other authors, who performed measurements with molten nitrate salts in enhanced tubes, the Ravigururajan correlation seems to overpredict the measured Nusselt numbers by a factor of 1.2 up to 1.4. This is, however within the uncertainty range of ±20% up to ±50% specified by Ravigururajan. Also, as can be seen in Fig. 10, the Ravigururajan correlation predicts a continuous increase of the Nusselt number ratio $Nu_{a,0}$ with the *Re* number. ($Nu_{a,0}$ increases 0.15 from *Re*=25,000 to 285,000). This can, given the present uncertainty of the high Reynolds number results, not be validated with the present measurements for *Re*>25,000.

Finally, Figs. 9 and 10 show the values expected by the general correlation for enhanced tubes proposed by Jiangfeng et al. [24]. This correlation was validated for *Re*=10,000 - 30,000, which roughly corresponds to Nu_m=100 – 300, so the values outside this interval must be considered with care. It can be observed that the general correlation of Jiangfeng predicts 62% of the measured values within ±5% and 91% of the measured values within ±10%. The deviations to the Jiangfeng correlation are found for *Re* numbers below 25,000. This is surprising, as the measurements of Jiangfeng were conducted with a spirally grooved tube which had a similar relative pitch angle for this Reynolds number range. However, Jiangfeng et al. used relative groove heights which were 30% larger and lower flux densities (~220 to 240 kW/m²). On the other hand, the relative groove width in the present experiment is 20% larger than the dimensions used by Jiangfeng and approaches values equal to one. Chen et al. [27] found that for a relative groove width equal to one, little to no increase of Nusselt number was observed.

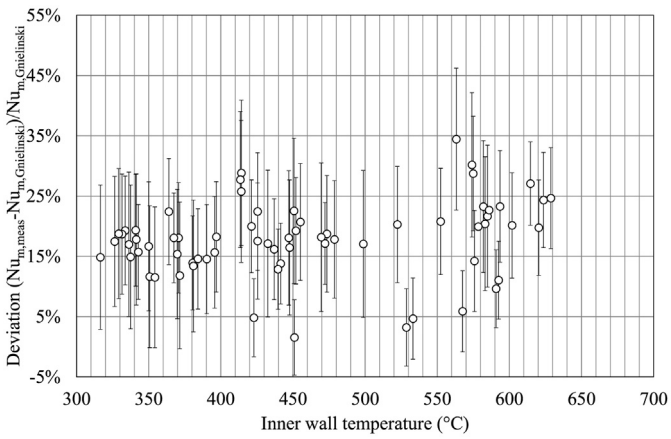

Fig. 11. Deviation of measured mean Nu number (spirally grooved tube) from the Gnielinski mean Nusselt number (smooth tube) as a function of the inner wall temperature (*Re*: 11,000…285,000; Pr: 3.7…10).

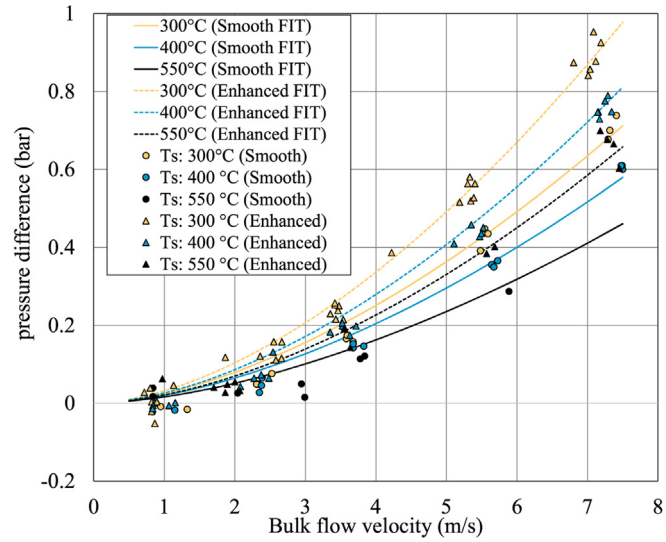

Fig. 12. Pressure difference over test section as a function of salt temperature for a smooth and the spirally enhanced tube (*Re*: 11,000…285,000; Pr: 3.7…10).

However, Chen's experiments were conducted for a transversally grooved tube. Also, it must be noted that both Chen and Jiangfeng used a ternary nitrate salt, which has Prandtl numbers which are roughly double the Pr numbers of the present binary nitrate salt. Furthermore, it could be argued, that the effect might be caused by local overheating of the salt.

Local salt degradation due to local overheating of the tube is a concern during the operation of heat exchangers using molten salts. This effect was observed by Jiangfeng et al. with the ternary nitrate salt Hitec [24]: They measured a rapid decrease of the convective heat transfer as the tube inner wall temperatures approached the maximum operation temperature specified by the manufacturer. This rapid decrease leads to further overheating of the tube and probably would entail further decrease of the heat transfer. Fig. 11 shows the deviation of the measured Nusselt number of the spirally grooved tube from the Nusselt number predicted by the Gnielinski correlation for a smooth tube. From this figure no obvious trend of the variation of Nusselt number compared to Gnielinski can be deduced as a function of inner wall temperature for T_{wi}=315 - 633 °C. However, some outliers can be observed; these measurements are obtained at low Reynolds numbers, which show a considerable reduction in heat transfer compared to the measurements at higher Nusselt numbers, as already seen in the previous graphs.

It can be concluded that inner wall temperatures up to 633 °C alone do not lead to a decrease in heat transfer in the present experiment. It must however be pointed out that the systematic decrease in heat transfer towards lower Reynolds numbers could be caused by local salt degradation. On the one hand, the salt has a higher dwell time in the tube at lower Reynolds numbers leaving more time for the gaseous products to form and disturbing the heat transfer. On the other hand, it could be, that beside the increase of local fluid velocity through the grooves, the grooves might also locally decrease the fluid velocity (for example shortly before and after the groove). This could cause local overheating beyond the measured inner wall temperatures and entail local salt degradation. The formation of a low conductive film can be excluded, because the low Reynolds number experiments were repeated at the very beginning and at the end of the measurement campaign and yielded the same results. Further research is necessary to quantify the observed Nusselt number behavior for *Re*= 10,000 to 25,000 in the spirally grooved tube and derive its origin with certainty. Furthermore, the present experiments were only carried out over a duration of a few weeks. Therefore, it cannot be excluded that long-term operation at high film temperatures would lead to the formation of a low conductance surface layer and to a local decrease of thermal conductivity of the tube. Further research is required to yield data in long-term operation.

7.2. Friction factor

In order to evaluate the performance enhancement properties of the spirally grooved tube, the friction factor ratio needs to evaluated beside the Nusselt number ratio. For this purpose, the pressure difference over the test section is deduced on one hand for the spirally grooved tube and on the other hand for a smooth tube using the same setup in a previous experiment [31]. Fig. 12 shows the measured pressure difference of the setup with a smooth tube and the setup with a spirally grooved tube for three bulk salt temperatures as a function of bulk flow velocity. It can be observed, that the pressure difference increases – as expected – in a quadratic fashion with increasing flow velocity. Also, the pressure difference decreases for higher temperatures, which is mainly due to the lower salt density at higher temperatures. In addition, it can be observed that the pressure difference of the spirally grooved tube is generally higher than for the smooth tube. It must be noted, that the pressure difference suffers from considerable scattering, for this reason only the measurement data for pressure differences greater than 0.3 bar will be evaluated further on. Fig. 13 shows the resulting friction factors deduced using Eq. (10). As expected, the friction factor decreases for higher Reynolds numbers and the friction factor of the spirally grooved tube is generally higher than that of the smooth tube. A power function is fitted to the measurement data following the basic form proposed by Blasius et al. for turbulent flow in a smooth tube [33] using a least square algorithm. Using these fitted functions, the friction factor ratio can be expressed using the following equation:

$$f_a/f_0 = \frac{0.7709 \cdot Re^{-0.3022}}{0.8843 \cdot Re^{-0.3415}} \tag{17}$$

It is interesting to point out that it was found, that correlations which account for roughness of the tube (Prandtl [40]) lead to lower agreement with the measurement data as these correlations predict a lower temperature-dependency as exposed by the measurement data. In this experiment the pressure difference of both the smooth and the enhanced tube are best predicted with correlations typically used for smooth tubes.

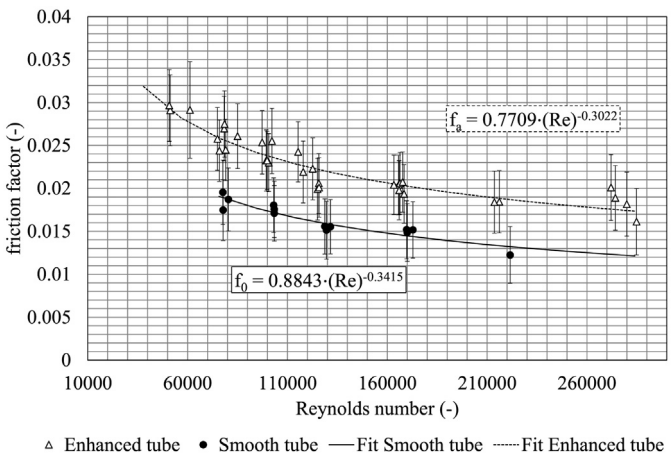

Fig. 13. Friction factor of the smooth and spirally grooved tube and respective fitted power functions as a function of Reynolds number.

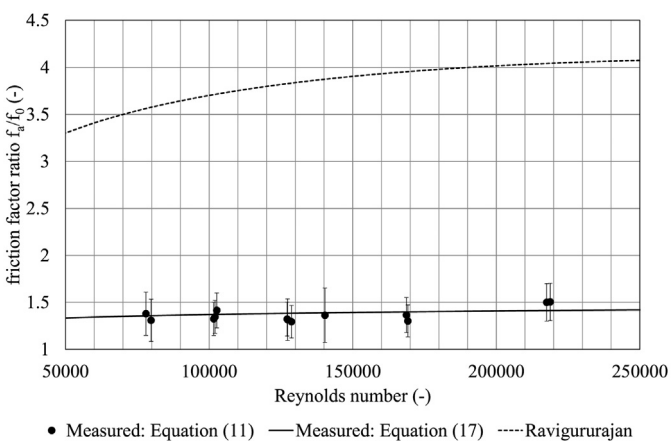

Fig. 14. Friction factor ratio deduced by two approaches from the measurement data and by a general correlation as a function of Reynolds number.

Fig. 14 shows the resulting friction factor ratio using Eq. (17) as well as the resulting friction factor when directly calculating the friction factor ratio using Eq. (11) from measurement data of the spirally grooved and smooth tube respectively. As not all measurements were taken at exactly the same salt temperature and Reynolds number only the useful pairs are shown. It can be seen, that the measurements achieved with this method (Eq. (11)) generally agree with the friction factors obtained with Eq. (17) within the measurement uncertainty. Furthermore, Fig. 14 shows the predicted friction factor ratio by the general equation by Ravigururajan et al. [10] The general correlation overpredicts the measured friction factor ratio by a factor of 1.8 to 2.9. This result lies considerably outside the uncertainty band given by Ravigururajan et al. of ±50%. The tube investigated in the present study has a groove height more at the lower end of the spectrum investigated by Ravigururajan et al., this might cause the overestimation, as the general correlations were developed to fit a large geometry basis. At the same time, the present results are in the same order of magnitude as the deviations measured by Chen et al. [27]. It must however be noted, that the measurements conducted by Chen are performed using a ternary nitrate salt, with a transversally grooved tube. Further research is necessary to understand the origin of this deviation. Further research is necessary to understand the causes of the deviation and to improve the predictions of pressure drops in enhanced tubes.

Conclusion

This paper experimentally analyses the forced convective heat transfer and pressure difference of the molten nitrate salt "Solar Salt" (60 wt-% $NaNO_3$; 40 wt-% KNO_3) in a spirally grooved tube at high Reynolds numbers at varying flux densities. In a first step a literature review on the experimentally available data of the thermo-hydraulic performance of corrugated tubes is performed. In a second step, the available data of corrugated tubes in nitrate salt heat exchangers is presented: it is found that the commonly used general correlations developed by Ravigururajan et al. [10] overpredict the experimental results of the Nusselt number of four different authors by 15% up to 90%. In addition, the general correlations for the friction factor ratio [10] overpredict the available experimental data by a factor of 1.7 up to 2.3. In the present work an experimental setup using a water-cooled induction heater is used to deduce the Nusselt number and the pressure difference over a test tube. The investigated spirally grooved tube has a relative groove height of e/2ri=0.017, a relative groove pitch of p/2ri =0.913 and a groove angle α=73.8° The measurements of the forced convective heat transfer are undertaken for three main bulk salt inlet temperatures: 300 °C, 400 °C and 550 °C, leading to Prandtl numbers ranging from 10 to 3.7. At each temperature up to 5 different mass flows are assessed. This approach leads to Reynolds numbers ranging between 11,000 and 285,000. Up to three different flux densities are applied for each combination of mass flow and temperature: 330 kW/m², 630 kW/m² and 930 kW/m². The measurement results of the spirally grooved tube are compared to previously published measurement results using the same measurement setup with a smooth circular tube.

The experiments yielding the friction factors shows that the general correlation of Ravigururajan for the friction factor ratio overpredicts the measured friction factor ratio by a factor of 1.8 to 2.9. This result lies considerably outside the uncertainty band of ±50% given by the authors of the general correlation. At the same time, the present results are in the same order of magnitude as the deviations measured by Chen et al. [27]. Further research is necessary to understand the origin of this deviation.

It is found, that for *Re* above 25,000, an increase of Nusselt number of roughly 1.19±0.14 is observed. However, the deduced Nusselt number ratios of the spirally enhanced tube are considerably lower than the values predicted by Ravigururajan's general correlations, but are still within the uncertainty range of ±20% up to ±50% specified for the general correlations. The measurements in the *Re* number region 11,000–25,000 show little to no increase of heat transfer for the spirally grooved tube compared to the smooth tube. This is in contradiction with the measurements conducted by other authors. Further research is necessary to identify the cause for this deviation.

One general concern with Solar Salt as a heat transfer fluid is that localized decomposition of the nitrate salt occurs in the film region with formation of gaseous products. This could form a local gas layer with low thermal conductivity and this layer could negatively impact the convective heat transfer of Solar Salt in heat exchanger tubes. The geometry of enhanced tubes does not only cause a local increase of fluid velocity but can also induce wakes and low-speed recirculation zones involving a local decrease in fluid velocity [8]. This could cause local overheating, entail local salt degradation and consequently impact the overall convective heat transfer. For this reason, special focus is put on the impact of inner tube wall temperatures larger than 600 °C on the heat transfer. Based on the measurements it can be concluded that inner wall temperatures up to 633 °C do not lead to a decrease in heat transfer in the present experiment. It must however be pointed out that the systematic decrease in heat transfer towards lower Reynolds numbers could be caused by local salt degradation. On

the one hand, the salt has a higher dwell time in the tube at lower Reynolds numbers leaving more time for gaseous products to form and disturbing the heat transfer. On the other hand, it could be that a local decrease in fluid velocity shortly before and after the groove caused local overheating and entailed local salt degradation. The formation of a low conductive film on the inner tube wall can be excluded, because the low Reynolds number experiments were repeated at the very beginning and at the end of the measurement campaign and yielded the same results. Further research is necessary to quantify the observed Nusselt number behavior for *Re*= 10,000 to 25,000 in the spirally grooved tube and define its origin with certainty. Furthermore, the present experiments were only carried out over a duration of a few weeks. Consequently, it cannot be excluded that long-term operation at high film temperatures would lead to the formation of a low conductance surface layer and to a local decrease of thermal conductivity of the tube. Further research is required to yield data in long-term operation.

Credit author statement

Cathy Frantz: Conceptualization, Methodology Software, Engineering, Measurement, Data curation, Writing.
Reiner Buck: Methodology, Supervision, Reviewing.
Marc Röger: Methodology, Supervision, Reviewing.
Bernhard Hoffschmidt: Supervision.

Declaration of Competing Interest

The authors declare that they have no known competing financial interests or personal relationships that could have appeared to influence the work reported in this paper.

Data availability

Data will be made available on request.

Acknowledgments

This work has been funded by the “German Federal Ministry for Economic Affairs and Energy” (0324327A).

References

[1] P. Falcone, A Handbook for Solar Central Receiver Design, Sandia National Laboratories Livermore SAND 86-8009, 1986.
[2] M. Mehos, C. Turchi, J. Vidal, C. Ho, A. Kruizenga and, et al., Concentrating Solar Power Gen3 Demonstration Roadmap, National Renewable Energy Laboratory, Golden, Colorado, 2017.
[3] D.C. Smith, Design and optimization of tube-type receiver panels for molten salt application, *Solar Engineering*, 2, ASME, 1992.
[4] A.K. Das, Heat transfer behavior of molten nitrate salt, AIP Conf. Proc. (SolarPACES) 1734 (2015) pp. 040003-1–040003-8.
[5] R. Uhlig, C. Frantz, R. Buck, Using corrugated tubes in external molten salt receivers, AIP Conf. Proc. 2126 (2019).
[6] A. Bonk and, et al., Influence of different atmospheres on molten salt chemistry and its effect on steel corrosion, AIP Conf. Proc. 2033 (2017) 090003.
[7] A. Bonk, M. Braun, V.A. Sötz, T. Bauer, Solar salt – pushing an old material for energy storage to a new limit, Appl. Energy 262 (2020).
[8] S.Z. Dizjeh, J. Brinkerhoff, Numerical investigations of turbulent heat transfer enhancement in circular tubes via modified internal profiles, Int. J. Thermofluids 16 (2022).
[9] A.E. Bergles, R.L. Webb, G.H. Junkhan, V. Nirmalan, Bibliography on Augmentation of Convective Heat and Mass Transfer - II, Iowa State Univesity, Ames, 1983.
[10] R.M. Manglik, et al., Chapter 11: enhancement of convective heat transfer, in: Handbook of Thermal Science and Engineering, Springer International Publishing AG, 2018, pp. 447–477.
[11] S.K. Saha and et al., Advances in Heat Transfer Enhancement, India: Springer briefs in applied sciences and technology, 2016.
[12] T.S. Ravigururajan, A.E. Bergles, Development and verification of general correlations for pressure drop and heat transfer in single-phase turbulent flow in enhanced tubes, Exp. Therm Fluid Sci. (1996) 55–70.
[13] G.Y. Min, The studies on the transversally corrugated tubes strengthening heat-transfer and resisting fouling in the evaporation station of sugar factory, J. Qiqihar Light Ind. Inst. 10 (1) (1994) 19–25.
[14] T.S. Ravigururajan, T.J. Rabas, Turbulent flow in integrally enhanced tubes, part 2: analysis and performance comparison, Heat Transf. Eng. 17 (2) (1996) 30–40.
[15] R.M. Manglik, A.E. Bergles, A.J. Dongaonkar, S. Rajendran, Limitations of compiling the global literature on enhanced heat and mass transfer, J. Enhanced Heat Transf. 20 (1) (2013) 83–92.
[16] R.I. Webb, Principles of Enhanced Heat Transfer, 1st ed., Wiley Interscience, New York, 1994.
[17] R.L. Webb, E.R.G. Eckert, R.J. Goldstein, Heat Transfer and friction in tubes with repeated-rib roughness, Int. J. Heat Mass Transfer 14 (4) (1971) 601–618.
[18] D.L. Gee, R.L. Webb, Forced convection heat transfer in helically rib-roughened tubes, Int. J. Heat Mass Transfer 23 (1980) 1127–1136.
[19] H.M. Li, K.S. Ye, Y.K. Tan, S.J. Deng, Investigation on tube-side flow visualization, friction factors and heat transfer characteristics of helical-ridging tubes, 7th Int. Heat Transf. Conf. 3 (1982) 75–80.
[20] A. García, P. Vicente, A. Viedma, Experimental study of heat transfer enhancement with wire coil inserts in laminar-transition-turbulent regimes at different Prandtl numbers, Int. J. Heat Mass Transf. 48 (2005) 4640–4651.
[21] W.-.T. Ji, A.M. Jacobi, Y.-.L. He, W.-.Q. Tao, Summary and evaluation on single-phase heat transfer enhancement techniques of liquid laminar and turbulent pipe flow, Int. J. Heat Mass Transf. 88 (2015) 735–754.
[22] J.F. Fan, W.K. Ding, J.F. Zhang, Y.L. He, W.Q. Tao, A performance evaluation plot of enhanced heat transfer techniques oriented for energy-saving, Int. J. Heat Mass Transf. 52 (2009) 33–44.
[23] W.-.T. Ji, A.M. Jacobi, Y.-.L. He, W.-.Q. Tao, Summary and evaluation on the heat transfer enhancement techniques of gas laminar and turbulent pipe flow, Int. J. Heat Mass Transf. 111 (2017) p. 67-483.
[24] L. Jianfeng and, et al., Convective heat transfer of high temperature molten salt in transversely grooved tube, Appl. Therm. Eng. 61 (2013) 157–162.
[25] L. Jiangfeng and, et al., Transition and turbulent convective heat transfer of molten salt in spirally grooved tube, Exp. Therm Fluid Sci. 47 (2013) 180–185.
[26] L. Jiangfeng and, et al., Enhanced heat transfer performances of molten salt receiver with spirally grooved pipe, Appl. Therm. Eng. 88 (2015) 491–498.
[27] C. Chen, Y.-.T. Wu, S.-.T. Wang, C.-f. Ma, Experimental investigation on enhanced heat transfer in transversally corrugated tube with molten salt, Exp. Therm Fluid Sci. 47 (2013) 108–116.
[28] S. Xiangyang and, et al., Enhanced heat transfer characteristics of molten salt in half-circumferentially heated horizontally corrugated tubes, CIESC J. 70 (12) (2019) 4546–4555.
[29] E.N. Sieder, G.E. Tate, Heat transfer and pressure drop of liquids in tubes, Ind. Eng. Chem. 28 (1936) 1429–1435.
[30] T. Bauer, N. Pfleger, N. Breidenbach, M. Eck, D. Laing, S. Kaesche, Material aspects of Solar Salt for sensible heat storage, Appl. Energy 111 (2013) 1114–1119 Volumepp. Pages.
[31] C. Frantz, R. Buck, M. Röger and B. Hoffschmidt, "Experimental analysis of forced convective heat transfer of nitrate salt in a circular tube at high Reynolds numbers and temperatures," *Int. J. Heat Mass Transf. Vol 201, Part 1 (2023)*.
[32] T.L. Bergman, A.S. Lavine, F.P. Incropera, D.P. Dewitt, Fundamentals of Heat and Mass Transfer, John Wiley & Sons, Inc., USA, 2011.
[33] V.D.I.V.-G.V.u. Chemieingenieurwesen, VDI-Wärmeatlas 10. Auflage, 2006.
[34] V. Gnielinski, Neue Gleichungen für den Wärme- und den Stoffübergang in turbulent durchströmten Rohren und Kanälen, Forsch. Gebiet Ingenieurwesens 41 (1) (1975) 8–16.
[35] A. Bonk, T. Bauer, Report on Thermo-Physical Properties of Binary NaNO3-KNO3 Mixtures in a Range of 59-61 wt% NaNO3, German Aerospace Center (DLR), Germany, 2021.
[36] A.H. Harvey, Reference correlations for thermophysical properties of liquid water at 0.1MPa," National Institute of Standards and Technology, J. Phys. Chem. Ref. Data 38 (1) (2009).
[37] T. Bauer, A. Bonk, Semi-empirical density estimations for binary, ternary and multicomponent alkali nitrate–nitrite molten salt mixtures, Int. J. Thermophys. (2018) 39–134.
[38] Q.-.G. Zhao and, et al., A theoretical model for predicting the thermal conductivity of binary molten salts, Int. J. Heat Mass Transf. 92 (2016) 639–642.
[39] G. Janz, Thermodynamic and transport properties for molten salts: correlated equations for critically evaluated density, surface tension, electrical conductance, and viscosity data, J. Phys. Chem. Ref. Data 17 (1988) 1–320 *(Supplement 2)*.
[40] L. Prandtl, Führer Durch Die Strömungslehre, 3. Auflage, 1950 Braunschweig.